Signature of point nodal superconductivity in the Dirac semimetal PdTe

C. S. Yadav [1,*] Sudeep Kumar Ghosh [2,†] Pankaj Kumar [1] A. Thamizhavel [3] and P. L. Paulose [3]

[1]*School of Physical Sciences, Indian Institute of Technology Mandi, Kamand, Mandi 175075 Himachal Pradesh, India*

[2]*Department of Physics, Indian Institute of Technology Kanpur, Kanpur 208016 Uttar Pradesh, India*

[3]*DCMP & MS, Tata Institute of Fundamental Research, Mumbai 400005 Maharashtra, India*

(Received 21 November 2023; revised 29 June 2024; accepted 30 July 2024; published 16 August 2024)

Recent angle-resolved photoemission spectroscopy (ARPES) experiments [Phys. Rev. Lett. **130**, 046402 (2023)] on PdTe, a 3D-Dirac semimetal and a superconductor with the transition temperature $T_c \sim 4.3$ K, have revealed compelling evidence of the presence of bulk nodes in the superconducting order parameter. To investigate the validity of this proposition, here we present a detailed investigation of the magnetic field dependence of the specific heat of PdTe down to temperatures ∼58 mK. We observed that the low-temperature specific heat of PdTe with an externally applied magnetic field exhibits a power-law field dependence, a characteristic of unconventional superconductivity. Furthermore, the zero-field low-temperature electronic specific heat follows a cubic temperature dependence, which is a signature of the presence of bulk point nodes in PdTe. These intriguing observations suggest that PdTe is a rare and fascinating topological material that exhibits both Dirac semimetallic properties and superconductivity with point nodal gap symmetry.

DOI: 10.1103/PhysRevB.110.054515

I. INTRODUCTION

Topological semimetals represent a fascinating class of materials characterized by topologically nontrivial bulk band crossings and robust surface states that exhibit unique electronic properties, making them highly desirable for practical applications [1]. The realm of topological semimetals becomes even more captivating when combined with superconductivity, as it opens up the possibility of realizing intrinsic topological superconductivity. Recent discoveries of materials exhibiting both topological semimetallic behavior and superconductivity have further bolstered this research direction, providing new avenues for exploring and understanding the intriguing interplay between topology and superconductivity. Examples include, superconducting 3D Dirac semimetals (Ta,Nb)OsSi [2], 3D Weyl semimetals LaPt(Si,Ge) [3], $\mathbb{Z}_2$ TMs (Cs,Rb,K)V_3Sb_5 [4,5], ZrOsSi [6], Weyl nodal-line SMs La(Ni,Pt)Si [7], and Kramers nodal-line SMs (Ti, Nb, Hf, Ta)RuSi [3].

Among the transition metal chalcogenides, FeSe shows unconventional superconductivity below ∼8.2 K. The scanning tunneling microscopy (STM) experiments on FeSe crystalline films suggested the existence of nodal superconductivity in stoichiometric FeSe [8]. Furthermore, the identification of C_4 rotation-symmetry protected Dirac semimetallic behavior, featuring distinctive surface Dirac cones, in the Fe(Se,Te) superconductors [9,10] has significantly advanced research in this class of materials. Several theoretical investigations [11–13] on these compounds have emphasized the potential for realizing various topological phases in Dirac semimetal superconductors. These phases include topological crystalline superconductivity [11], nodal higher-order topological superconductivity [12], and novel gapped superconducting state with surface Bogoliubov-Dirac cones and a second-order time-reversal invariant topological superconductor with helical Majorana hinge modes [13]. Recent angle-resolved photoemission spectroscopy (ARPES) measurements [14] provide compelling evidence that the chalcogenide superconductor PdTe exemplifies such intriguing material characteristics as well.

PdTe is a hexagonal superconductor with $T_c \sim 4.3$ K [15–17] that has a layered structure similar to that of the tetragonal Fe chalcogenide superconductors. However, the 4*d*-orbital character of Pd and the face-shared octahedral environment suppress electronic correlations and promote three-dimensionality in PdTe [18,19]. This enhanced three-dimensionality, in turn, gives rise to weaker Fermi surface nesting and diminished long-range correlations [18]. Based on first principles calculations, it was proposed that there is a diminished charge transfer energy between Pd-*d* and Te-*p* states in PdTe when compared to Fe chalcogenides. The Pd-*d* states in PdTe are almost fully occupied, leaving no states available to form a large Hund's moment and there is no long-ranged magnetic correlations present in PdTe [18].

In recent ARPES measurements on PdTe [14], a noteworthy revelation emerged that a bulk Dirac point is situated just below the Fermi level accompanied by Fermi arc surface states on the (010) surface. These investigations also uncovered compelling evidence of a rare phenomenon: the coexistence of nodeless superconductivity on the surface and nodal superconductivity in the bulk of PdTe. Inspired by the distinctive characteristics exhibited by this material, here we embarked on comprehensive field- and temperature-dependent investigations of the heat capacity of PdTe, down

*Contact author: shekhar@iitmandi.ac.in

†Contact author: skghosh@iitk.ac.in

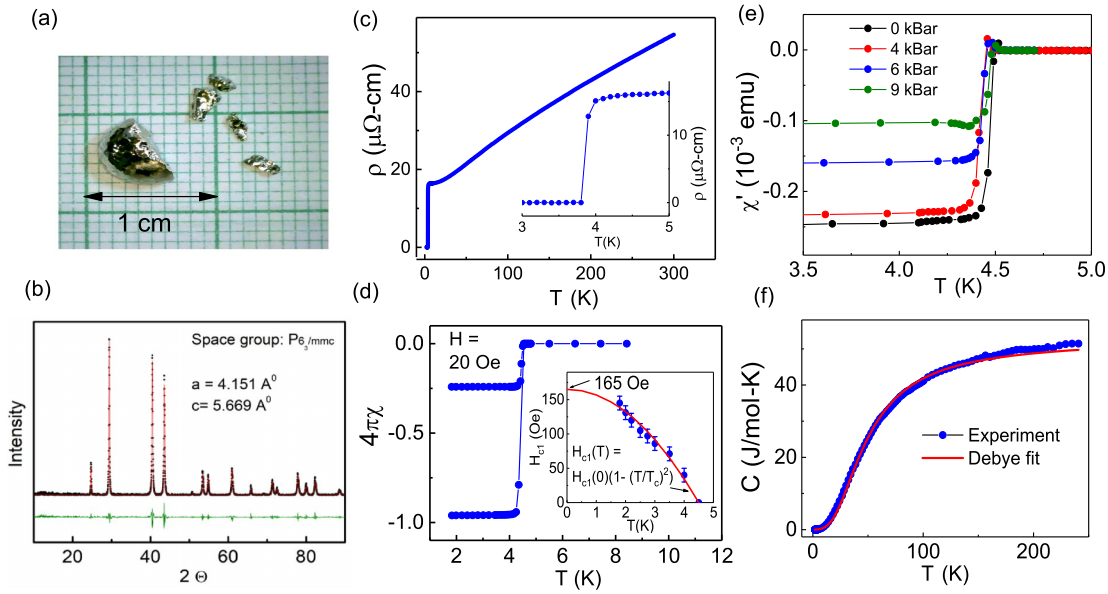

FIG. 1. Characterization of PdTe samples. (a) An image of the PdTe ingot showing the shiny nature of crystallites. (b) XRD pattern of powdered PdTe sample showing a clean hexagonal phase (space group: P6$_3$/*mmc*). (c) The temperature dependence of the electrical resistivity. The inset shows a zoomed region around the superconducting transition ($1.8 \leqslant T \leqslant 5$ K). (d) DC magnetic susceptibility as a function of temperature at $H = 20$ Oe. The inset shows $H_{c1}(T)$ obtained from the M-H isotherms, and the fit with $H_{c1}(T) = H_{c1}(0)(1 - (T/T_C)^2)$. (e) AC magnetic susceptibility measured at different external hydrostatic pressures $p = 0$, 4, 6, and 9 kbar. (f) Total specific heat $C(T)$ fitted with the Debye model [Eq. (1)].

to ultralow temperatures (∼58 mK). We found that the zero-field electronic specific heat data at these low temperatures in the superconducting state align remarkably well with the Bardeen-Cooper-Schrieffer (BCS)-type model featuring a p-wave gap symmetry with point nodes in the bulk. Furthermore, our findings gain additional support from the magnetic field dependence of the electronic heat capacity, which distinctly points toward the unconventional nature of superconductivity in PdTe.

II. RESULTS AND DISCUSSION

PdTe samples were prepared by solid-state reaction method using high purity ($\geqslant 99.9\%$) Pd and Te powders inside an evacuated quartz tubes at 1080 °C for 24 hours. The ingot were found to consist of large crystallites of 1–2 mm size as shown in Fig. 1(a). The Rietveld refinement of the x-ray diffraction (XRD) data shown in Fig. 1(b) revealed the formation of a clean NiAs-type hexagonal phase in PdTe with the space group symmetry P6$_3$/*mmc* (No. 194) and with the lattice parameters, $a = 4.15$ Å and $c = 5.67$ Å.

The electrical characterizations (under an ac current 10 mA at frequency 79 Hz) and the heat capacity measurements were performed using a Physical Properties measurement System (PPMS), and the magnetic measurements were performed using a Magnetic property measurement system (SQUID-MPMS). The temperature dependence of the electrical resistivity $\rho(T)$ of PdTe is shown in Fig. 1(c). A sharp superconducting transition is observed at $T \sim 4.3$ K [inset of Fig. 1(c)], with the full diamagnetic signal ($4\pi\chi = -1$) as shown in Fig. 1(d). We note that $\rho(T)$ follows normal Fermi liquid behavior [$\rho(T) \propto T^2$] up to temperatures ∼42 K, which is more than the 1/5th of the Debye-temperature ($\Theta_D \sim 200$ K) of PdTe. The inset of Fig. 1(d) shows temperature dependence of the lower critical field [$H_{c1}(T)$] obtained from the M-H isotherms. Fitting of $H_{c1}(T)$ curve with the empirical relation $H_{c1}(T) = H_{c1}(0)(1 - (T/T_C)^2)$ gives $H_{c1}(0) \approx 165 \pm 10$ Oe, which is slightly lower than the reported value (≈200 Oe) [17].

The AC susceptibility data measured at different externally applied hydrostatic pressures $p = 0$, 4, 6, and 8 kbar are shown in Fig. 1(e). We note that the T_c of PdTe gets suppressed with increasing pressure ($\Delta T_c/\Delta p \sim -0.01$ K/kbar). The low value of the coefficient of the suppression of T_c of PdTe with p may imply that its density of states (DOS) is nearly flat at the Fermi energy. This is consistent with the band structure calculations showing that the Fermi energy is located very close to the local maxima of the DOS [18]. The decrease in T_c with pressure for PdTe contrasts with unusually large p dependence on T_c shown by the Fe chalcogenide superconductors [20]. Note that the high-pressure AC susceptibility measurements were conducted using a pressure cell, making it challenging to calculate the sample's exact demagnetization factor. While we could not estimate the precise superconducting volume fraction under pressure, the data clearly indicates that it decreases as pressure increases.

The variation of the total heat capacity (C) in zero magnetic field with temperature for PdTe is shown in shown in the Fig. 1(f). We note that in the normal state at high temperatures the specific saturates to $C(T = 250\ \text{K}) \sim 50$ J mole^{-1} K^{-1}, which is close to classical Dulong-Petit limit of $C = 3nR = 6R = 49.9$ J mole^{-1} K^{-1} due to the lattice vibrations, as expected. The low-T normal state heat capacity data is fitted with a combination of the electronic and lattice contributions

(Debye model of specific heat) using the expression [21]

$$C = \gamma T + 9nR\left(\frac{T}{\Theta_D}\right)^3 \int_0^y \frac{x^4 e^x}{(e^x-1)^2} dx, \qquad (1)$$

where $y = \Theta_D/T$ and Θ_D is the Debye Temperature. The best possible fit gives the Sommerfeld coefficient $\gamma \sim 6.32$ mJ mole^{-1} K^{-2} and $\Theta_D \sim 200$ K. The values of γ in normal state, obtained from the low Temperature linear fit of C/T versus T^2 data is also ~6.30 mJ mole^{-1} K^{-2}. The DOS at Fermi energy N(E$_F$) obtained using the relation $\gamma = \pi^2 k_B^2 N(E_F)/3$ is $N(E_F) \sim 2.67$ states/(eV f.u.). This DOS $N(E_F)$ contains the enhancement factor due to electron-phonon coupling constant $\lambda_{\text{el-ph}}$, and can be related to the bare-band DOS at the Fermi level $N_0(E_F)$ by the expression $N(E_F) = N_0(E_F)(1 + \lambda_{\text{el-ph}})$. The calculated value of the $\lambda_{\text{el-ph}}$ using the MacMillan's theory, corresponding to $\Theta_D = 200$ K is $\lambda_{\text{el-ph}} \sim 0.7$, which is similar to that of a weak coupling BCS superconductor [22]. However, considering the modified Macmillan formula with the logarithmic averaged phonon frequency it was reported that $\lambda_{\text{el-ph}} \approx 1.4$ in Ref. [15].

Further, we estimate the Fermi velocity v_F in PdTe from the $N(E_F)$ using a single band free electron gas model as $v_F = \frac{\pi^2\hbar^3}{m^{*2}V_{\text{f.u.}}} N(E_F)$, where $V_{f.u.} = V_{\text{cell}}/2$ [21]. Assuming m* = m$_e$, we have $v_F = 4.8 \times 10^8$ cm/sec. The mean free path $l = v_F\ \tau$, (τ = mean relaxation time) obtained using the formula $l = 3\pi^2(\frac{\hbar}{e^2\rho_0})(\frac{\hbar}{m^* v_F})^2$ is estimated to be $l \sim 43.8$ nm [21]. This is an order of magnitude smaller than $l = 305.4$ nm (estimated using $l = (2\text{m}_e v_F)/(\text{ne}^2\rho_0)$, where n is carrier concentration obtained from Hall measurement and ρ_0 is the resistivity at $T = 2$ K [15]) corresponding to the $v_F \sim 7 \times 10^7$ cm/sec estimated by considering the bare band density of states obtained from the band structure calculation reported in Ref. [15].

Now, we focus on the low-temperature ($T \sim 0.058$–6 K) behavior of the specific heat $C(T)$ in externally applied magnetic fields. The variation of the specific heat in this regime as a function of temperature for different magnetic fields up to ~1200 Oe are shown in the Fig. 2(a). The gradual suppression of the peak height and of T_c in the presence of magnetic field is clearly evident from this figure. The variation of the upper critical field $H_{c2}(T)$ with temperature is shown in the inset of Fig. 2(a). We have fitted this $H_{c2}(T)$ versus T data using the generalized Ginzburg-Landau (GL) equation: $H_{c2}(T) = H_{c2}(0)[(1-t^2)/(1+t^2)]$ [23–25], where $t = T/T_c$ is the reduced temperature, the zero-temperature upper critical field is $H_{c2}(0)$, and T_c is 4.47 K. The value of $H_{c2}(0)$ as obtained from the fit is $H_{c2}(0) = 1473.16$ Oe. Further, we have extracted the zero-temperature orbital limited upper critical field $H_{c2}^{\text{orb}}(0)$ from the Werthamer-Helfand-Hohenberg formula given as $\mu_0 H_{c2}(0) = -0.693 T_c (\mu_0 dH_{c2}/dT)_{T=T_c}$ [26]. The calculated value of $\mu_0 H_{c2}(0)$ is 1332 Oe, which is lower than 1473.155 Oe, obtained from the GL fit. The coherence length ξ calculated using $\xi = (\phi_0/(2\pi\mu_0 H_{c2}))^{1/2} \sim 47.2$ nm, which is close to the mean free path $l \sim 43.8$ nm of PdTe indicating that PdTe is close to the dirty limit [27,28].

We have extracted the relative electronic specific heat defined as

$$\Delta\gamma(H) = \lim_{T\to 0}\left[\frac{C(H,T)}{T} - \frac{C(H=0,T)}{T}\right] \qquad (2)$$

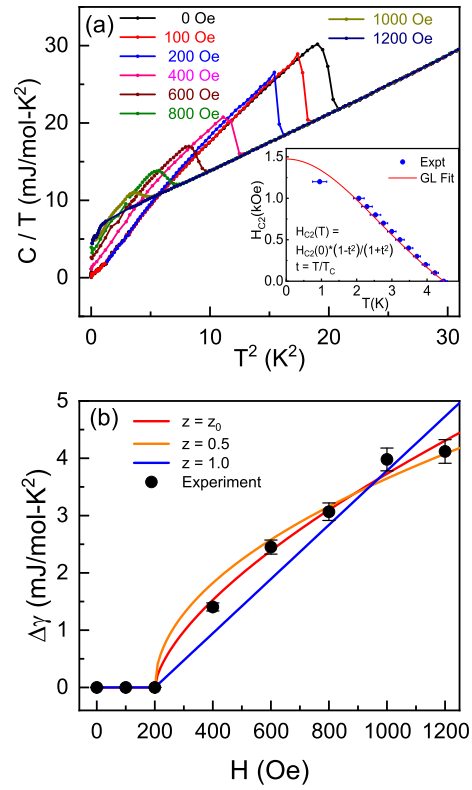

FIG. 2. Field dependence of specific heat. (a) Variation of the total specific heat (C) with temperature at various magnetic fields: $H = 0$–1200 Oe, The inset shows the temperature of the upper critical field H_{c2}. The dashed red line in the inset shows a fitting of the H_{c2} data using the generalized Ginzburg-Landau equation: $H_{c2}(T) = H_{c2}(0)[(1-t^2)/(1+t^2)]$ [23–25]. (b) Magnetic field dependence of the relative electronic specific heat $\Delta\gamma$ given by Eq. (2). The fittings shown are with the form $\Delta\gamma \propto (H - H_0)^z$ in the mixed state of PdTe for $H > H_0$ with $H_0 \approx H_{c1}(0)$. The best is fit found with the exponent $z = z_0 = 0.644 \pm 0.059$ which is clearly different from the linear ($z = 1$) and square-root ($z = 0.5$) dependencies shown.

from the low-temperature specific heat data [shown in Fig. 2(a)] at different magnetic fields. The field dependence of $\Delta\gamma(H)$ for type-II superconductors in the mixed state is expected to be $\propto$H for a conventional s-wave BCS gap and a power law $\propto H^z$ with $0.5 < z < 1$ for an unconventional gap symmetry in general [29–32] with $z = 0.5$ usually implying the presence of line nodes in the order parameter for a two dimensional material [29,30]. The variation of $\Delta\gamma(H)$ with the applied magnetic fields in the mixed state of the PdTe superconductor is shown in Fig. 2(b). We have fitted the data for $\Delta\gamma(H)$ in the mixed state for $200 \lesssim H \lesssim 1200$ Oe by a power law $\sim(H - H_0)^z$ for $H > H_0$, where $H_0 \approx H_{c1}(0)$. We find a good fit with the exponent $z = 0.644 \pm 0.059$ as shown in Fig. 2(b). Such a power law field dependence of $\Delta\gamma(H)$ clearly points to the unconventional nature of superconductivity in PdTe consistent with previously reported results [17]. However, to clearly determine the nature and position of the nodes in the superconducting gap, orientation-dependent measurements of the low-temperature specific heat using good quality single crystals are needed [33,34].

The low-temperature total specific heat data $C_{\text{total}}(T)$ in the zero field of PdTe in the normal state ($T_c \leqslant T \leqslant 10$ K) are

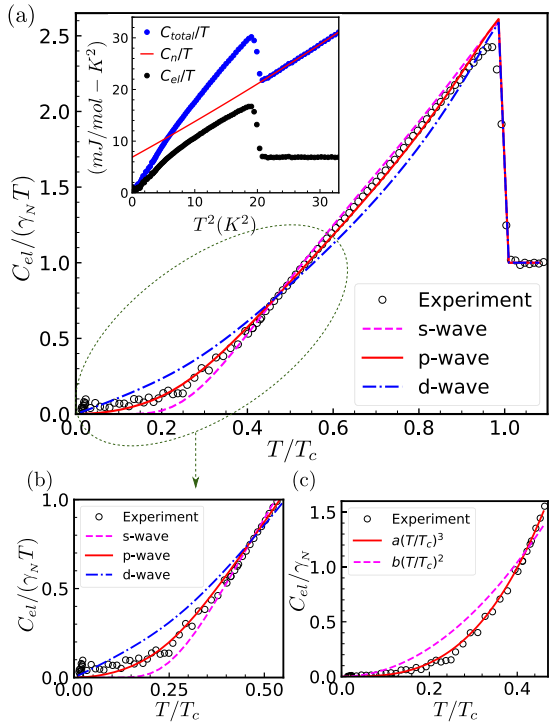

FIG. 3. Zero-field electronic specific heat. (a) The electronic specific heat (C_{el}) data as a function of temperature without any external field present. The experimental data is fitted with three different models of the order parameter: a fully gapped s-wave BCS (pink), a point nodal p-wave (red) and a line-node dominated d-wave (blue). The inset shows behavior of the total specific heat (C_{total}), the total specific heat in the normal state (C_n) extrapolated to zero temperature and the electronic specific heat (C_{el}) obtained after subtracting the phonon contribution from C_{total}. (b) The zoom of the marked low-temperature region of the specific heat figure in (a). We note that clearly the p-wave model fits the specific heat data much better throughout the temperature window than the other two models. (c) The low-temperature specific heat shows a clear $\sim T^3$ temperature dependence characteristic of the presence of bulk point nodes as in the p-wave model. Here, the values of the constant parameters used in the fitting are $a = 15.49$ and $b = 6.51$.

fitted with the form $C_n(T) = \gamma_N T + C_{ph}$, where the first term is the electronic contribution to the specific heat in the normal state and the second term is the phononic contribution to the specific heat $C_{ph} = \beta T^3 + \delta T^5$. The fitting shown in the inset of Fig. 3(a) gives $\gamma_N = 6.303$ mJ mole^{-1} K^{-2}, $\beta = 0.748$ mJ mole^{-1} K^{-4}, and $\delta = 0.0019$ mJ mole^{-1} K^{-6} for PdTe. Then we extract the low-temperature electronic specific heat (C_{el}) data of PdTe by defining $C_{el}(T) = C_{total}(T) - C_{ph}(T)$. The variation of the C_{el}(T) at zero field ($H = 0$) at low temperatures is shown in the Fig. 3. The low-temperature behavior of C_{el} can be used to investigate symmetry of the superconducting gap realized in a particular material. To this end, we have defined $\gamma_e(T) = C_{el}/T$ and fitted it with a generalized single-band BCS-type form applicable for different types of superconducting gap symmetries given by [35]

$$\gamma_e = \frac{N(E_F)}{2k_B T^3}\left\langle \int_0^\infty d\epsilon \,\mathrm{sech}^2\left(\frac{E_k}{k_B T}\right)\left[E_k^2 - \frac{T}{2}\frac{d\Delta_k^2(T)}{dT}\right]\right\rangle_{FS}, \quad (3)$$

where $E_k = \sqrt{\epsilon^2 + \Delta_k^2(T)}$ and $\langle \ldots \rangle_{FS}$ represents an average over the Fermi surface (assumed to be spherical). The gap function ($\Delta_k(T)$) defined as $\Delta_k(T) = \Delta'(T)g(k)$ has a universal temperature dependence $\Delta'(T) = \Delta_0 \tanh[1.82\{1.018(T_c/T - 1)^{0.51}\}]$ and all the information about its symmetry is contained in the function $g(k) = g(\theta, \phi)$ with θ and ϕ being azimuthal and polar angles, respectively [36]. Then for a particular gap symmetry we would have only one fitting parameter $\frac{\Delta_0}{k_B T_c}$ in Eq. (3). In an s-wave superconductor, the isotropic gap at the Fermi surface leads to the exponential decay of the electronic specific heat on decreasing temperature. However, this behavior of the electronic specific heat gets affected by the presence of nodes in the superconducting gap at the Fermi surface and for $T < T_c$ a power-law decay of electronic specific heat is observed that goes as $\propto T^2$ for line nodes and $\propto T^3$ in the presence of point nodes [37–39].

We have fitted the experimental data of C_{el} for PdTe by the form given in Eq. (3) assuming a spherical Fermi surface, for three different types of models corresponding to the superconducting gap symmetries: (i) s-wave with $g(k) = 1$ having a full gap, (ii) p-wave with $g(k) = \sin(\theta)$ having only point nodes, and (iii) d-wave with $g(k) = \sin(2\theta)$ having a line node at the equator ($\theta = \pi/2$) that dominates the low-temperature behavior [36]. We first make sure that the jump at T_c in the electronic specific heat is accurately reproduced from all the fitted models. The fittings of C_{el}/T versus T, which enables us to look into the low-temperature region carefully, are shown in Fig. 3(a). We note from this Fig. 3(a) that the specific heat behaves as a power-law expected for a nodal order parameter instead of being exponentially suppressed expected for a fully gapped order parameter as a function of temperature in the low-temperature region $0 \leqslant T/T_c \lesssim 1/3$. As a result, the s-wave does not give good fit to the data. The d-wave model also gives a poor fitting while a reasonably good fit to the experimental electronic specific heat data throughout the temperature range was obtained for the p-wave superconducting gap function. To exemplify the low-temperature behavior of the specific heat we have also shown a zoomed version of Fig. 3(a) in Fig. 3(b). The values of the fitting parameter $\frac{\Delta_0}{k_B T_c}$ for the s-, p-, and d-wave models shown in Fig. 3 are $\sim$1.83, $\sim$2.29, and $\sim$2.56, respectively. Hence, we conclude that the electronic specific heat of PdTe is well described by a weak-coupling p-wave generalized BCS-type order parameter with $\frac{\Delta_0}{k_B T_c} \sim 2.29$ which is close to the conventional weak-coupling BCS value $\sim$1.76. This conclusion is further validated by explicitly fitting the low-temperature behavior of the specific heat with temperature power laws expected for the nodal order parameters as shown in the Fig. 3(c). We note that there is a clear $\sim T^3$ temperature dependence in the region $0 \leqslant T/T_c \leqslant 1/3$ characteristic of the presence of bulk point nodes in the superconducting order parameter of PdTe. This $C_{el} \propto T^3$ dependence at low temperatures for PdTe is quite remarkable and conforms with the evidence of the bulk point nodes in the superconducting order parameter reported based on ARPES measurements [14].

PdTe is a multiband superconductor with the point group D_{6h} which has both nondegenerate and degenerate irreducible representations. As a result, several symmetry allowed

single- and multicomponent superconducting order parameters are allowed in PdTe and in general it is difficult to clearly identify which superconducting instability channel is realized in PdTe. However, mean-field calculations using a Slater-Koster type tight-binding model for PdTe, considering only the p_x and p_y orbitals of Te and the effect of spin-orbit coupling such that the type-I Dirac crossing observed in ARPES along the Γ-A direction is qualitatively captured, also suggest that a superconducting gap function with a bulk point node is indeed possible in PdTe even in the most symmetric superconducting instability channel [14].

The jump in the electronic specific heat (ΔC) at T_c in zero field ($H = 0$) for PdTe shown in the Fig. 3(a) is $\Delta C/(\gamma_N T_c) \approx 1.49$ which is also similar to the weak coupling BCS value ∼1.43 [22]. Our finding is consistent with previous studies $\Delta C/(\gamma_N T_c) \approx 1.33$ [17] and ≈1.67 [15] but a little less compared to the value ≈2.1 reported in Ref. [19]. The value of $\Delta C/(\gamma_N T_c)$ can, however, depend on the sample quality and the superconducting volume fraction in the samples. Moreover, some superconductors such as many of the cuprate and Fe-chalcogenide superconductors do not exhibit jump in the specific heat as well [40–42]. We note that the electronic specific heat data of PdTe was reported to be fitted with an unconventional two-gap s-wave type model in Ref. [19] where the corresponding samples had at least ∼16% nonsuperconducting volume fraction. We also note that another recent work on PdTe reported multigap behavior from thermal conductivity data [43]. However, the thermal conductivity data may not be able to properly determine the nodal superconducting behavior due to the corresponding small size and irregular shapes of PdTe single crystals used [43].

III. SUMMARY AND CONCLUSION

Nodal superconducting materials [36,44–46] represent a rare and intriguing class of unconventional superconductors, captivating the interest of researchers seeking to unravel their nature and pairing mechanisms. Based on recent angle-resolved photoemission spectroscopy (ARPES) measurements [14], it was proposed that PdTe, a 3D Dirac semimetal in its normal state, also exhibits point nodal superconductivity in the bulk. To verify the unconventional nature of superconducting order parameter in PdTe, we have conducted extensive field- and temperature-dependent specific heat measurements in the mixed state of PdTe.

In our field dependent specific heat data, we have observed a power-law field dependence in the specific heat that deviates from the usual linear behavior expected for an isotropic fully gapped order parameter [32]. Our zero-field specific heat data offers additional insights, remarkably revealing a clear $\sim T^3$ temperature dependence in the low-temperature regime ($T < T_c/3$) that strongly suggests the presence of bulk point nodes in the superconducting order parameter of PdTe. Notably, a weak-coupling BCS-type superconducting order parameter with point nodes yields an excellent fit to the zero-field specific heat data throughout the temperature range. Thus our bulk specific heat measurements in the superconducting state of the 3D Dirac semimetal PdTe point towards its rare identification as a point nodal superconductor as proposed in Ref. [14].

PdTe stands out as a unique 3D Dirac semimetal material [14] because it (i) features Dirac points near the Fermi level, (ii) has an accessible transition temperature (T_c), (iii) is cleavable to measure superconducting Fermi arc states, and (iv) has unconventional point nodal superconducting ground state. Further confirmation of the point nodal superconducting order parameter in PdTe will require the use of complementary experimental techniques, such as solid-state nuclear magnetic resonance (NMR) to measure spin susceptibility [47] and tunnel-diode oscillator (TDO) to measure the London penetration depth [48] in combination with orientation-dependent measurements with good quality single crystals [33,34].

ACKNOWLEDGMENTS

C.S.Y. acknowledges SERB-DST (India) for the CRG Grant (CRG/2021/002743). Advanced Material Research Center (AMRC), IIT Mandi is acknowledged for the experimental facility. S.K.G. gratefully acknowledges financial support from SERB, Government of India via the Startup Research Grant: SRG/2023/000934, as well as from IIT Kanpur through the Initiation Grant (IITK/PHY/2022116). The authors also acknowledge Dibyendu Samanta for discussions.

[1] B. Q. Lv, T. Qian, and H. Ding, Experimental perspective on three-dimensional topological semimetals, Rev. Mod. Phys. **93**, 025002 (2021).

[2] S. K. Ghosh, P. K. Biswas, C. Xu, B. Li, J. Z. Zhao, A. D. Hillier, and X. Xu, Time-reversal symmetry breaking superconductivity in three-dimensional Dirac semimetallic silicides, Phys. Rev. Res. **4**, L012031 (2022).

[3] T. Shang, J. Zhao, L.-H. Hu, J. Ma, D. J. Gawryluk, X. Zhu, H. Zhang, Z. Zhen, B. Yu, Y. Xu, Q. Zhan, E. Pomjakushina, M. Shi, and T. Shiroka, Unconventional superconductivity in topological kramers nodal-line semimetals, Sci. Adv. **8**, eabq6589 (2022).

[4] K. Jiang, T. Wu, J.-X. Yin, Z. Wang, M. Z. Hasan, S. D. Wilson, X. Chen, and J. Hu, Kagome superconductors AV_3Sb_5 (A = K, Rb, Cs), Natl. Sci. Rev. **10**, nwac199 (2023).

[5] Z. Shan, P. K. Biswas, S. K. Ghosh, T. Tula, A. D. Hillier, D. Adroja, S. Cottrell, G.-H. Cao, Y. Liu, X. Xu, Y. Song, H. Yuan, and M. Smidman, Muon spin relaxation study of the layered kagome superconductor CsV_3Sb_5, Phys. Rev. Res. **4**, 033145 (2022).

[6] S. K. Ghosh, B. Li, C. Xu, A. D. Hillier, P. K. Biswas, X. Xu, and T. Shiroka, ZrOsSi: a Z_2 topological metal with a superconducting ground state, Front. Phys. **11**, 1256166 (2023).

[7] T. Shang, S. K. Ghosh, M. Smidman, D. J. Gawryluk, C. Baines, A. Wang, W. Xie, Y. Chen, M. O. Ajeesh, M. Nicklas *et al.*, Spin-triplet superconductivity in Weyl nodal-line semimetals, npj Quantum Mater. **7**, 35 (2022).

[8] C.-L. Song, Y.-L. Wang, P. Cheng, Y.-P. Jiang, W. Li, T. Zhang, Z. Li, K. He, L. Wang, J.-F. Jia, H.-H. Hung, C. Wu, X. Ma, X. Chen, and Q.-K. Xue, Direct observation of nodes and twofold symmetry in FeSe superconductor, Science **332**, 1410 (2011).

[9] P. Zhang, K. Yaji, T. Hashimoto, Y. Ota, T. Kondo, K. Okazaki, Z. Wang, J. Wen, G. D. Gu, H. Ding, and S. Shin, Observation of topological superconductivity on the surface of an iron-based superconductor, Science **360**, 182 (2018).

[10] P. Zhang, Z. Wang, X. Wu, K. Yaji, Y. Ishida, Y. Kohama, G. Dai, Y. Sun, C. Bareille, K. Kuroda *et al.*, Multiple topological states in iron-based superconductors, Nat. Phys. **15**, 41 (2019).

[11] T. Kawakami and M. Sato, Topological crystalline superconductivity in Dirac semimetal phase of iron-based superconductors, Phys. Rev. B **100**, 094520 (2019).

[12] Z. Wu and Y. Wang, Nodal higher-order topological superconductivity from a C_4-symmetric Dirac semimetal, Phys. Rev. B **106**, 214510 (2022).

[13] M. Kheirkhah, Z.-Y. Zhuang, J. Maciejko, and Z. Yan, Surface Bogoliubov-Dirac cones and helical Majorana hinge modes in superconducting Dirac semimetals, Phys. Rev. B **105**, 014509 (2022).

[14] X. P. Yang, Y. Zhong, S. Mardanya, T. A. Cochran, R. Chapai, A. Mine, J. Zhang, J. Sánchez-Barriga, Z.-J. Cheng, O. J. Clark *et al.*, Coexistence of bulk-nodal and surface-nodeless Cooper pairings in a superconducting Dirac semimetal, Phys. Rev. Lett. **130**, 046402 (2023).

[15] A. B. Karki, D. A. Browne, S. Stadler, J. Li, and R. Jin, PdTe: A strongly coupled superconductor, J. Phys.: Condens. Matter **24**, 055701 (2012).

[16] A. B. Karki, V. O. Garlea, R. Custelcean, S. Stadler, E. Plummer, and R. Jin, Interplay between superconductivity and magnetism in $Fe_{1-x}Pd_xTe$, Proc. Natl. Acad. Sci. USA **110**, 9283 (2013).

[17] B. Tiwari, R. Goyal, R. Jha, A. Dixit, and V. P. S. Awana, PdTe: a 4.5 K type-II BCS superconductor, Supercond. Sci. Technol. **28**, 055008 (2015).

[18] C. E. Ekuma, C.-H. Lin, J. Moreno, W. Ku, and M. Jarrell, First-principles Wannier function analysis of the electronic structure of PdTe: weaker magnetism and superconductivity, J. Phys.: Condens. Matter **25**, 405601 (2013).

[19] R. Chapai, P. S. Reddy, L. Xing, D. E. Graf, A. B. Karki, T.-R. Chang, and R. Jin, Evidence for unconventional superconductivity and nontrivial topology in PdTe, Sci. Rep. **13**, 6824 (2023).

[20] D. C. Johnston, The puzzle of high temperature superconductivity in layered iron pnictides and chalcogenides, Adv. Phys. **59**, 803 (2010).

[21] C. Kittel, *Introduction to Solid State Physics*, 8th ed. (Wiley, 2004)

[22] W. L. McMillan, Transition temperature of strong-coupled superconductors, Phys. Rev. **167**, 331 (1968).

[23] K. Maki, Effect of Pauli paramagnetism on magnetic properties of high-field superconductors, Phys. Rev. **148**, 362 (1966).

[24] N. R. Werthamer, E. Helfand, and P. C. Hohenberg, Temperature and purity dependence of the superconducting critical field, H_{c2}. III. electron spin and spin-orbit effects, Phys. Rev. **147**, 295 (1966).

[25] L. Fang, Y. Wang, P. Y. Zou, L. Tang, Z. Xu, H. Chen, C. Dong, L. Shan, and H. H. Wen, Fabrication and superconductivity of Na_xTaS_2 crystals, Phys. Rev. B **72**, 014534 (2005).

[26] N. Momono and M. Ido, Evidence for nodes in the superconducting gap of $La_{2-x}Sr_xCuO_4$– T^2 dependence of electronic specific heat and impurity effects, Physica C: Superconductivity **264**, 311 (1996).

[27] C. S. Yadav and P. L. Paulose, Upper critical field, lower critical field and critical current density of $FeTe_{0.60}Se_{0.40}$ single crystals, New J. Phys. **11**, 103046 (2009).

[28] A. Pourret, L. Malone, A. B. Antunes, C. S. Yadav, P. L. Paulose, B. Fauqué, and K. Behnia, Strong correlation and low carrier density in $Fe_{1+y}Te_{0.6}Se_{0.4}$ as seen from its thermoelectric response, Phys. Rev. B **83**, 020504 (2011).

[29] G. E. Volovik, Superconductivity with lines of GAP nodes: density of states in the vortex, Sov. Phys. JETP **58**, 469 (1993).

[30] N. Nakai, P. Miranović, M. Ichioka, and K. Machida, Field dependence of the zero-energy density of states around vortices in an anisotropic-gap superconductor, Phys. Rev. B **70**, 100503 (2004).

[31] Y. Bang, Volovik effect in the $\pm s$-wave state for the iron-based superconductors, Phys. Rev. Lett. **104**, 217001 (2010).

[32] M. Zehetmayer, A review of two-band superconductivity: materials and effects on the thermodynamic and reversible mixed-state properties, Supercond. Sci. Technol. **26**, 043001 (2013).

[33] P. Miranović, N. Nakai, M. Ichioka, and K. Machida, Orientational field dependence of low-lying excitations in the mixed state of unconventional superconductors, Phys. Rev. B **68**, 052501 (2003).

[34] I. Vekhter, P. J. Hirschfeld, J. P. Carbotte, and E. J. Nicol, Anisotropic thermodynamics of d-wave superconductors in the vortex state, Phys. Rev. B **59**, R9023 (1999).

[35] J. Xing, H. Lin, Y. Li, S. Li, X. Zhu, H. Yang, and H.-H. Wen, Nodal superconducting gap in tetragonal FeS, Phys. Rev. B **93**, 104520 (2016).

[36] P. K. Biswas, S. K. Ghosh, J. Zhao, D. A. Mayoh, N. Zhigadlo, X. Xu, C. Baines, A. Hillier, G. Balakrishnan, and M. Lees, Chiral singlet superconductivity in the weakly correlated metal $LaPt_3P$, Nat. Commun. **12**, 2504 (2021).

[37] G. Goll, *Unconventional Superconductors: Experimental Investigation of the Order-Parameter Symmetry* (Springer Science & Business Media, 2006), Vol. 214.

[38] D. Pines and P. Monthoux, $d_{x^2-y^2}$ pairing and spin fluctuations in the cuprate superconductors: A progress report, J. Phys. Chem. Solids **56**, 1651 (1995).

[39] S. K. Ghosh, M. Smidman, T. Shang, J. F. Annett, A. D. Hillier, J. Quintanilla, and H. Yuan, Recent progress on superconductors with time-reversal symmetry breaking, J. Phys.: Condens. Matter **33**, 033001 (2021).

[40] L. Ding, C. He, J. K. Dong, T. Wu, R. H. Liu, X. H. Chen, and S. Y. Li, Specific heat of the iron-based high-T_c superconductor $SmO_{1-x}F_xFeAs$, Phys. Rev. B **77**, 180510 (2008).

[41] M. Tropeano, A. Martinelli, A. Palenzona, E. Bellingeri, E. Galleani d'Agliano, T. D. Nguyen, M. Affronte, and M. Putti, Thermal properties of $SmFeAsO_{1-x}F_x$ as a probe of the

interplay between electrons and phonons, Phys. Rev. B **78**, 094518 (2008).

[42] W. Schnelle, N. Knauf, J. Bock, E. Preisler, and J. Hüdepohl, The specific heat anomaly of $Bi_2Sr_2CaCu_2O_{8+\delta}$ at Tc in dependence on the oxygen content, Physica C: Superconductivity **209**, 456 (1993).

[43] C. Zhao, X. Liu, J. Wang, C. Xu, B. Wang, W. Xia, Z. Yu, X. Jin, X. Zhang, J. Wang, D. Dai, C. Tu, J. Nie, H. Wang, Y. Jiao, D. Duong, S. Huang, R. Jin, Z. Xu, Y. Guo *et al.*, Multigap nodeless superconductivity in the topological semimetal pdte, Phys. Rev. B **109**, 174502 (2024).

[44] W. J. Gannon, W. P. Halperin, C. Rastovski, K. J. Schlesinger, J. Hlevyack, M. R. Eskildsen, A. B. Vorontsov, J. Gavilano, U. Gasser, and G. Nagy, Nodal gap structure and order parameter symmetry of the unconventional superconductor UPt_3, New J. Phys. **17**, 023041 (2015).

[45] A. Bhattacharyya, D. T. Adroja, K. Panda, S. Saha, T. Das, A. J. S. Machado, O. V. Cigarroa, T. W. Grant, Z. Fisk, A. D. Hillier, and P. Manfrinetti, Evidence of a nodal line in the superconducting gap symmetry of noncentrosymmetric $ThCoC_2$, Phys. Rev. Lett. **122**, 147001 (2019).

[46] T. Shang, M. Smidman, A. Wang, L.-J. Chang, C. Baines, M. K. Lee, Z. Y. Nie, G. M. Pang, W. Xie, W. B. Jiang, M. Shi, M. Medarde, T. Shiroka, and H. Q. Yuan, Simultaneous nodal superconductivity and time-reversal symmetry breaking in the noncentrosymmetric superconductor CaPtAs, Phys. Rev. Lett. **124**, 207001 (2020).

[47] D. F. Smith and C. P. Slichter, The study of mechanisms of superconductivity by NMR relaxation, in *Novel NMR and EPR Techniques*, edited by J. Dolinšek, M. Vilfan, and S. Žumer (Springer, Berlin, Heidelberg, 2006), pp. 243–295.

[48] R. Giannetta, A. Carrington, and R. Prozorov, London penetration depth measurements using tunnel diode resonators, J. Low Temp. Phys. **208**, 119 (2022).